Large eddy simulation applied to study the influence of upstream conditions in a backward-facing step flow

Jean-Luc Aider* and Alexandra Danet

Department of Research and Innovation,

PSA Peugeot-Citroën, 2 route de Gisy,

78943 Vélizy-Villacoublay, France. †

Marcel Lesieur

LEGI - Equipe MoST - Boite Postale 53 - 38041 Grenoble cedex 09 - Fance.

(Dated: October 9, 2006)

Abstract

We use Large Eddy Simulation (LES) to investigate the influence of upstream boundary conditions on the development of turbulent structures downstream of a backward-facing step. The first inlet condition consists of a mean turbulent profile perturbed by a white noise. The second relies upon a more realistic condition, in which fully turbulent inflow data are derived from an auxiliary simulation of a quasi-temporal boundary layer. Pressure and velocity statistics, supplemented by visualizations, demonstrate how the flow in the shear layer is strongly influenced by the upstream conditions. The turbulent boundary-layer trigger a rapid destabilization of the mixing layer, resulting in a shortening of the recirculation length. Analysis of the temporal spectra show that the precursor simulation leads to an increase of the characteristic frequencies associated to the Kelvin-Helmholtz (KH) vortices and to the flapping of the shear layer. Streaks and quasi-longitudinal vortices created in the turbulent boundary layer induce high and low longitudinal velocity modulations upstream of the step edge. The spanwise modulation of the velocity seems to be responsible for the wavy destabilization of the KH vortices. The dependency of the mean flow and of the characteristic frequencies of pressure fluctuations to the incoming boundary layer clearly demonstrates the importance of defining as realistic boundary conditions as possible for the simulation of complex 3D flows or for flow control simulations. One finds also in this work a review of averaged and temporal characteristics of the flow over a backward-facing step.

PACS numbers: 47.27.Ep, 47.27.De, 47.27.N-, 47.32.Ff

Keywords: Large Eddy Simulation, Backward-Facing Step

*Electronic address: aider@pmmh.espci.fr

†Also at Physique et Mécanique des Milieux Hétérogènes, Ecole Supérieure de Physique et Chimie Industrielles (PMMH UMR 7636-CNRS-ESPCI), 10 rue Vauquelin, 75231 Paris Cedex 5, France.

I. INTRODUCTION

A Direct Numerical Simulation (DNS) or even a Large Eddy Simulation (LES) of the flow over a road vehicle is still impossible, even if one can see few examples of LES computations over simplified vehicle models like the Ahmed body [1]. On the other hand, a LES computation of the flow in a sub-domain of the vehicle, where the flow is strongly time-dependent, is possible. Nevertheless, even if we know the mean flow and the Reynolds stress in the main domain (from a Reynolds Averaged Navier-Stokes computation or from experimental measurements) we still have the problem of the choice of the right perturbations for the inlet of the LES sub-domain [2]. This is the same problem as for any time-dependent computations: one has to define realistic time-dependent inlet conditions.

The influence of inlet conditions, if properly defined, can be visible further downstream. The definition of the boundary conditions, especially for a spatially-developing flow, is then very important and also a pretty difficult task. Previous works have considered the influence of upstream conditions on downstream evolution of a turbulent flow (Isomoto et al. [3], Keating et al. [4]). Isomoto [3], for instance, studied how the turbulence intensity imposed at the inlet of the computation domain modifies the recirculation length downstream of a backward-facing step. According to them, the turbulence close to the wall ($y^+ < 50$) plays a major role in the modification of the reattachment process.

When we define the inflow conditions of a computational domain, one can mainly use two types of data: random or synthetic fluctuations trying to mimic turbulence, or a precursor computation used to generate a realistic turbulent flow.

To generate artificial inflow conditions, one can add random temporal fluctuations $u(\mathbf{x}, t)$ with controlled amplitude to a mean velocity profile $U(\mathbf{x})$:

$$\mathcal{U}(\mathbf{x}, t) = U(\mathbf{x}) + u(\mathbf{x}, t)$$

The mean velocity profile can be obtained from a RANS computation or experimental measurements. Silveira et al. [5] used a white noise with a small amplitude to mimic the residual turbulence at the inlet of the domain of a backward-facing step. The same amount of energy is used for each frequency. This method was successful in the case of transitional flows like boundary [6] or mixing layers [7].

To obtain more realistic fluctuations different options have been used. One can for in-

stance generate the fluctuations using a predetermined energy spectrum corresponding to isotropic turbulence [8]. Thanks to the "Frozen Turbulence" hypothesis, one can extract the inlet plane of a decaying compressible turbulence. The method was also used for wall bounded flows like a backward-facing step flow [9].

Nevertheless, in spite of a proper Reynolds stress tensor, the phase randomization of the fluctuations destroys the coherent structures. The spatio-temporal coherence appears to be an essential aspect [10] and implies the existence of a relaxation zone where the flow recreates the coherence, which makes the computation longer and more expensive. One can also discuss the validity of the Taylor hypothesis in the case of wall-bounded flows [11].

The destruction of the periodicity can also be obtained through the jamming of the amplitude of the initial fluctuations spectrum [12, 13]. It seems that this method is more attractive than the phase jamming for wall bounded flows, because it does not kill the turbulent structures. A relaxation zone is still necessary but not as big as in the the phase case.

A method has been developed to simulate a boundary layer with a null or favorable pressure gradient [14]. One of the hypotheses is that the flow is weakly inhomogeneous in the main direction. It also introduces a multi-scale approximation which allows for the computation of the spatial evolution of the boundary layer with periodic conditions. Spalart and Watmuff [15] proposed a similar method for boundary layer with adverse pressure gradient. In a periodic computation, they define three zones : one main zone and two border zones on each side of the main zone ("fringe method"). The first "fringe zone" is the one where the inflow conditions are generated, while the second "fringe zone" is a buffer zone at the outlet of the domain. In the "fringe zones" one can add arbitrary terms to modify the boundary layer, while in the main zone the Navier-Stokes equation are not modified.

Another way to obtain realistic inflow boundary conditions is to run a simulation for the upstream flow. The main advantage of this method is that it gives the right temporal and spatial informations.

Friedrich and Arnal [16] computed the fully turbulent flow in a periodic straight duct. The sub-grid model, the spatial resolution and the time-step are the same as in the "successor" domain. A plane perpendicular to the flow is then extracted and used as an inlet conditions for a backward-facing step flow. Their results are in a good agreement with the experimental data.

Another method, using both the precursor and Taylor hypothesis, has been proposed [13]. The precursor is a periodic turbulent channel flow. For a given time-step, all the planes at each longitudinal position are used as inlet conditions for the successor domain, which is a spatially developing channel flow. The precursor domain is swept with a convection velocity using the Taylor hypothesis. The time-dependent computation is realized for another time step ΔT and a new set of data is recorded. ΔT is the most important parameter and should be chosen carefully. In practice $\Delta T \geq h/U_\tau$ which is the time scale related to the large scale structures created in the channel flow, h being the channel height and U_τ the friction velocity. On the other hand, if ΔT is too large, the method becomes equivalent to the "classic" precursor computation. This method finally seems to be more efficient than the amplitude jamming [12] because the transition zone is much smaller and does not show the periodicity traces characteristic of the methods using a predetermined spectrum.

More recently, another method has been applied to a mixing layer flow [17]. The two layers are generated by a precursor computation of a time-dependent boundary layer. A unique time series of length ΔT (the integral scale of the target flow), is acquired before being transformed in periodic conditions. It can then be used as much as necessary as inlet conditions of the spatial domain. The periodicity imposed at the domain inlet does not modify the mixing layer: the authors show that the periodicity quickly vanishes thanks to the non-linear interactions of the flow. The method, efficient for the mixing layer, should still be tested for a wall bounded flow.

An interesting method is given for a precursor computation of a boundary layer: thanks to the classical laws of the boundary layer, the inlet velocities are evaluated from the outlet data [18]. As it is one of the methods we will use, it will be detailed in the following sections.

The different methods using "precursor domains" appear to be the most efficient to generate realistic inflow conditions. Keating et al.[4] recently tested different inflow conditions for large-eddy simulations of a spatially developing turbulent channel flow. They showed the important role of large scales and also demonstrated the efficiency of realistic time and phase informations for the development of turbulence. Precursor simulations were clearly among the most efficient methods to generate realistic turbulent flows. Nevertheless they are limited to a few simplified geometries. Moreover, another problem has been underlined [16]: in some cases, the downstream flow can interact with the upstream flow. The physical separation between upstream and downstream flows prevents any retroaction between the

different regions of the flow.

To finish with this review, one should mention another method that cannot be associated with any of the two main strategies previously discussed. Its objective is to develop an efficient interface between experiments and simulations. Thanks to the Reynolds Stress tensor and a few physical probes in the flow, one could reconstruct the total signal using the Linear Stochastic Estimation (LSE) [10]. One can use the Proper Orthogonal Decomposition (POD) in the 3D cases. The flow field generated through these methods can then be used as inlet conditions for the numerical simulation. It has been applied successfully in the case of a 2D mixing layer. The role of the simulation as a "turbulence regenerator" from the limited data used to reconstruct the flow fields was also emphasized.

In the following section we present the numerical procedure and the computational domain. In the third section, we describe the two artificial upstream boundary conditions used. Then we study the mean flow and averaged quantities obtained with the two different inflow conditions and show how they are modified. Finally we study the time-dependent flow and the spectral signatures of the vortical structures. The influence of the upstream boundary condition is also clearly emphasized and thoroughly analyzed. The incoming boundary layer is also analyzed in details to explain the modification of the mean flow and of the different characteristic frequencies.

II. PROBLEM SPECIFICATION

A. Filtered equation and LES model

The governing equations are the compressible Navier-Stokes equations expressed in the conservative form. The system is filtered with an implicit spatial filter using the Favre decomposition [20]. To close the set of equations obtained through filtering, the subgrid stress tensor and the subgrid heat flux have to be prescribed.

The model applied in this study is based on the eddy-viscosity concept using as a starting point the second-order Structure Functions of the resolved velocity field. The model for the anisotropic part of the subgrid stress tensor has in this case the following expression:

$$\mathcal{T}_{ij} = 2\nu_t S_{ij} \tag{1}$$

where the eddy viscosity introduced ν_t writes :

$$\nu_t(x,t) = C_{sf}\Delta\sqrt{\overline{F}_{2,\Delta}(x,t)}, C_{s,f} = 0.105C_K^{-3/2} \tag{2}$$

This approach has been proposed by [19]. We use an extension of this model, the Filtered Structure-Function model, developed by [6, 20] in its four points version. The objective of this extension is to reduce the weight of large-scale velocity gradients when determining the structure function. This is achieved by applying a low-pass filter to the velocity field before computing its structure function.

B. Numerical domain and procedure

The parameters defining the main numerical domain used for the computations are listed in table 1. The three coordinates x, y, z, represent respectively the longitudinal, cross-stream and spanwise directions. The origin of the longitudinal axis $x = 0$ is taken at the edge of the step. All quantities are normalized by the step height h and the free-stream longitudinal velocity U_o imposed at the inlet of the domain (Fig.1).

The computational domain consists of an inlet section $L_e = 2.5h$ prior to the sudden expansion which extends over $L_x = 18h$. The dimensions in the other directions are respectively $(L_y, L_z) = (6h, 4h)$. The expansion ratio $Er = H_2/H_1$, i.e. the ratio between the domain height downstream and upstream of the step is 1.2 . The corresponding Reynolds number based on the step height is $Re_h = 5100$. The Mach number is $Ma = 0.3$, and the boundary-layer thickness at the inlet of the computational domain $\delta_{99} \approx 1.2h$.

All these dimensions and the corresponding Reynolds number are the same as in the DNS of Le et al. [9]. The Mach number is small enough so that the flow is only weakly compressible. Our results can then be compared to other incompressible experiments [21] or simulations [9].

We use a structured mesh, with a uniform grid in the spanwise direction. In the vertical and longitudinal directions the mesh is refined in the strong shear flow regions i.e. close to the walls and downstream of the step edge. Grid spacing are expressed in wall coordinates based on the inlet boundary layer shear velocity $U_{\tau o}$. As we will see later we use data obtained from a flat plate turbulent boundary layer calculation of Spalart [14] where $U_{\tau o} = 4.910^{-2}U_o$.

Present calculations were performed with a multi-domain compressible code using MacCormack finite difference numerical method. The scheme is second-order accurate in time and fourth-order in space (see [22] and also [23]).

A no-slip boundary condition is used along the lower wall. In the spanwise direction, where turbulence is assumed to be statistically homogenous, we impose periodic boundary conditions. Other boundaries are treated with the non-reflective boundary condition method proposed by [24], [25].

We use two different inflow boundary conditions. The first one is a mean vertical boundary layer profile perturbed by a white noise (WN). The second is the result from a precursor simulation (PS). The two will be described in details in the following sections.

The upper boundary of the domains has been treated the same way as the exit, i.e. a free outlet frontier (FO). The influence of this frontier on the upstream and downstream flow has been investigated by comparing with a free slip condition (FS). Our computations showed that the FS condition is responsible for the creation of a longitudinal pressure gradient in the downstream relaxation zone which modifies strongly the structure of the flow (the recirculation bubble is increased, for instance). We do not detail these computations as we will focus in the following on the computations with the free outlet upper frontier. Nevertheless we stress that FS conditions were used by Le and Moin [9] for their incompressible DNS of a backward-facing step within the same configuration. This point is to be remembered when we will compare our results to their DNS.

In table I we summarize the grid characteristics, inflow and upper boundaries conditions tested for the two simulations: the white noise (WN) and precursor simulation (PS).

III. UPSTREAM CONDITIONS

A. White noise

The first inlet condition used in this study consists of a mean turbulent profile perturbed by a white noise. The longitudinal mean velocity is fitted to the profile of the Direct Numerical Simulation of a turbulent boundary layer computed by Spalart [14] with a Reynolds number $Re_\theta = 670$ ($Re^*_\delta = 1000$). Here θ is the momentum thickness and $\delta_{99} = 6.1\delta^*$. The vertical and spanwise components of the mean velocity are set to zero. At each time step

random fluctuations are superimposed on the inflow profile. The maximum intensity of the noise is set to 1.5 U_o and is applied in the region where $y \leq \delta_{99}$. Some computations showed us that it is not necessary to keep Spalart's turbulence intensity profiles [14] (15%U_o). As noticed by Fureby [26] the results are insensitive to the level of prescribed fluctuations. In fact, the lack of spatial and temporal correlations leads to a sharp drop in intensity in the few nodes following the inlet. Thus we observe a turbulent longitudinal velocity profile, without any structures and associated energy, close to the separation region as shown by the contours of longitudinal velocity in a X plane just upstream of the step edge (Fig.2-a).

B. Precursor simulation

The second method used to generate time-dependent turbulent inflow data is the one proposed by Lund et al. [18]. It consists of an auxiliary simulation which generates its own inflow conditions through a sequence of operations where the velocity field at a downstream station is re-scaled and re-introduced at the inlet of the precursor domain. This method produces a realistic turbulent boundary layer leading to statistics that are in good agreement with target profiles previously presented. A selected vertical plane at the exit of this precursor domain is then extracted, stored and used afterwards as inflow conditions for the step domain (figure 3). The computational domain of the precursor required about 350 000 grid points for the following dimensions $(L_x, L_y, L_z) = (10h, 5h, 4h)$ and a grid resolution corresponding to the main domain. The recycling position X_{recy} where the data are stored was set to $8h$.

On figure 4 the boundary layer profile is compared with Spalart's [14]. We note on Fig. 4(a) a slight acceleration in the logarithmic zone which seems to be related to the computational method. The same behavior was observed in Lund et al. results [18]. The overestimation of the longitudinal velocity is clearly an effect of weak near wall resolution, insufficient to resolve properly the wall velocity gradient. Nevertheless, in this case, the inflow conditions present a turbulent mean longitudinal velocity containing coherent structures and corresponding energies.

The differences observed in the velocity profiles are also confirmed in the isocontours of the longitudinal velocity field (figure 2-b)) and the velocity-vectors projection in the same cross-section (figure 5). The precursor simulation is clearly efficient in creating a

strongly turbulent boundary layer exhibiting counter-rotating longitudinal vortices, as shown on figure 6 through isosurfaces of Q-criterion. These longitudinal vortices, which cannot be observed in the WN simulation, modify the base flow with a spanwise modulation of the velocity field.

If we look in the precursor domain at an instantaneous contour of longitudinal velocity fluctuations in an horizontal plane close to the wall ($y^+ \simeq 12$), we can clearly see the trace of coherent longitudinal vortices (figure 7). We will see in the following how these structures seem to generate natural perturbations at the step edge modifying the downstream flow.

IV. QUALITATIVE DESCRIPTION OF THE FLOW DOWNSTREAM OF THE BACKWARD-FACING STEP

A. Qualitative description of the structure of the flow

We first recall briefly the main features of the backward-facing step flow. As mentioned earlier, the geometry is simple but exhibits a very complex flow (figure 8). The first phenomenon is the separation occurring at the edge of the step. The separation is imposed by the geometry, which makes the simulation a little easier but we still need a very good grid to define properly the mixing layer developing spatially downstream of the edge. The mixing layer grows further downstream and gives rise to spanwise vortices (Kelvin-Helmholtz vortices) that will then go through a destabilization process whose dynamics is complex and inherently time dependent. The step geometry forces the mixing layer to reattach on the wall surface at the bottom. This phenomenon leads to the creation of a recirculation region between the reattachment line and the step edge, inducing a flow moving in the upstream direction. The recirculation bubble and the mixing layer are both time-dependent with different natural frequencies.

B. Qualitative analysis of the influence of the upstream boundary condition

In the previous section we have observed a strong modulation of the velocity field in the upstream domain in the PS case. We can search now for evidence of the influence of this modulation on the vortices created downstream of the step edge.

On figure 9 we show a 3D view of the instantaneous velocity field for the two simulations. The qualitative differences between the two simulations are obvious. One can notice in particular how the mixing layer downstream of the step becomes quickly unstable in the PS case compared to the WN case. The same kind of difference can be observed in the temporal evolution of isosurface of the Q-criterion, as shown on the two animations 2-5 and 2-6 presented in Lesieur et al. [20] and that can be downloaded on the website of the editor. This is illustrated by the snapshot given in figure 10. In particular one can see the creation of spanwise Kelvin-Helmholtz vortices just downstream of the edge in both cases. In the PS case, the KH vortices becomes wavy more quickly and one can see the creation of hairpin vortices further downstream. From these two visualizations, one can expect strong differences between the two simulations for both averaged and temporal characteristics.

V. INFLUENCE OF UPSTREAM CONDITIONS ON AVERAGED QUANTITIES

A. Derivation of the mean quantities

In this section we study the modifications of the mean flow by the upstream conditions downstream of the step edge. We will examine various mean quantities in addition to the traditional recirculation length. All the statistics that will be presented in the following have been obtained by averaging the pressure and velocity field *both in time and space* (in the spanwise direction). The statistical sampling starts after the initial transients and during 200 non-dimensionalized time $t_{stat} \approx 220h/U_o$. The transient time is determined rigorously by computing the cumulative average of the recirculation length and of the longitudinal velocity recorded in three probes located downstream of the separation.

B. Surface parameters

We first compute the mean wall shear stress coefficient C_f:

$$C_f = \frac{\tau_w}{\frac{1}{2}\rho U_o^2} \tag{3}$$

where $\tau_w = \rho U_\tau^2$ is the shear stress at the wall. $U_\tau = U_o\sqrt{(\nu\frac{\partial U}{\partial y})_{wall}}$ is the shear stress velocity.

We compare on Fig. 11 the C_f mean longitudinal profiles downstream of the step obtained with our computations, to Le et al. DNS [9], and to Jovic and Driver experiment [21]. The positions where the profiles vanish define the recirculation length of the separation bubble downstream of the step. We find a recirculation length $X_r = 5.80$ for the WN simulation and $X_r = 5.29$ for the PS case. The recirculation length is clearly decreased and the intensity of the minimum of C_f increased when the incoming boundary layer contains turbulent eddies. The recirculation bubble is then shorter and more intense in the more realistic case. We also notice that the peak of negative stress coefficient compares very well with the experimental results.

This result is also well illustrated on Fig. 12 by the streamlines contours for the two simulations. The recirculation bubble is clearly decreased in the more realistic case. We can also notice the secondary recirculation close to the step. The decrease of X_r seems to be associated with the decrease of the size of the secondary recirculation.

If we compare with other results, we obtain a smaller recirculation length than in the incompressible DNS of Le et al. [9] ($X_r \simeq 6.28h$) and slightly smaller than in the experiments of Jovic and Driver [21] ($X_r \simeq 6h \pm 0.15$). This result is a little surprising, if we refer to the work of Kuehn [27] who showed that the recirculation length is increased when the expansion ratio is increased. If we consider that our outflow condition on the upper boundary can be seen as an infinite expansion ratio, we should get a larger recirculation length. Nevertheless we emphasize once again the differences in the upper and upstream boundary conditions with the experiment of Jovic and Driver and computations of Le et al.. We will see that it can induce some modifications of the velocity field that can explain the modification of the recirculation length.

In the following, we may employ the normalized longitudinal coordinates $X = \frac{x - X_r}{X_r}$.

We can also compare the normalized wall pressure coefficient $\widetilde{C}_p$:

$$\widetilde{C}_p = \frac{C_p - C_{p,min}}{1 - C_{p,min}} \quad , \quad \text{where} \quad C_p = \frac{p - p_o}{\frac{1}{2}\rho U_o^2} \tag{4}$$

obtained in our two simulations against Driver et al. experiment [28]. The three profiles are displayed on Fig. 13. One can see that our simulations compare well with the experiment until we reach the step edge. After this point we slightly overestimate the pressure coefficient in the two simulations. The strong adverse pressure gradient region followed by the favorable

pressure gradient zone are still very similar to the one observed by Chandrsuda and Bradshaw [29] and Driver et al. [28].

C. Mean velocities

On the figures 14(a) and 14(b) we show the longitudinal evolution of, respectively, the mean longitudinal and mean vertical velocity. The three longitudinal positions correspond to the center of the recirculation bubble ($X = -0.36$), the reattachment region ($X = -0.05$) and the relaxation zone ($X = 0.6$).

The differences are relatively small between our two simulations for the two velocity components. The WN condition induces a slight acceleration of the longitudinal velocity profile and a weaker vertical velocity in the recirculation compared to the PS case.

The comparison with the experimental profiles of Jovic and Driver [21] and the numerical results of Le et al. [9] is more interesting. Our computations lead to a slightly accelerated longitudinal velocity profiles compared with the experimental results, while the DNS of Le et al. fits remarkably well with the experimental profiles. On the contrary, one can see a strong discrepancy between the numerical results and the experimental vertical velocity profiles. The DNS of Le et al. underestimates the vertical velocity in the region close to the wall ($y < h$) and overestimates it when $y > h$. Our computations lead to a relatively good estimation of the vertical velocity in the region close to the wall (the PS case being better than the WN case), but we strongly overestimate the vertical velocity when $y > h$, even compared to the DNS of Le et al. [9]. This can be explained by the different upper boundary conditions. As mentioned earlier, we use an outflow boundary condition on the upper part of the numerical domain, so that we do not force the vertical velocity. This is very different from the experimental setup of Jovic and Driver [21], where upper part of the test section is closed with a symmetric backward-facing step. To be closer to the experiment, we should have used a symmetry conditions for the upper boundary. This is also different from the DNS of Le et al. [9] where the upper boundary is a no-stress wall with a $v = 0$ condition. We believe that this overall downward vertical velocity could explain why we obtain a smaller recirculation length in our simulations. This downward vertical velocity can also explain the overestimation of the friction coefficient in the relaxation region observed in Fig. 11. For the above-stated reasons, our simulations might be closer to real detachments occurring in

aerodynamics of cars and subsonic airplanes.

D. Turbulence intensities

We first compare on Fig. 15 the turbulence intensity profiles for the three velocity components ($(\overline{u'^2})^{1/2}$, $(\overline{v'^2})^{1/2}$, $(\overline{w'^2})^{1/2}$) and the Reynolds shear stress component $\overline{u'v'}$ to the experimental measurements of Jovic and Driver [21] and to the DNS of Le et al [9].

The rms profiles of longitudinal velocity fluctuations obtained with the PS case compare very well with the experimental profiles of Jovic and Driver [21], for the three longitudinal position, shown in Fig. 15(a). The WN case underestimates the velocity fluctuations in the region between the step edge and the reattachment point.

The vertical velocity fluctuations are also well predicted by the PS case, even if the DNS of Le et al. [9] shows a better agreement (Fig. 15(b)). Once again, the WN case predicts poorly the vertical velocity fluctuations. In the region between the step edge and the reattachment point, the WN case clearly overestimates the velocity fluctuations in the region close to the wall ($y < h$).

For the spanwise velocity fluctuations, shown in Fig. 15(c), the results can only be compared to the DNS of Le et al. [9]. The precursor simulation gives also a better agreement with the DNS than the White Noise case.

Finally, we see on Fig. 15(d) that both the PS and WN cases predict poorly the maximum of the Reynolds shear stress component $\overline{u'v'}$. The vertical extent of the profile is relatively well predicted by the PS simulation which fits very well the experimental data for $y < 0.2h$ and $y > 1.2h$. In these regions, the PS case gives even better results than the DNS of Le et al. [9].

We can also compare the longitudinal evolution, downstream of the step, of the maxima of longitudinal and vertical turbulence intensities obtained in our two simulations. The results are shown on Fig. 16(a) and 16(b). We observe that the longitudinal velocity fluctuations (Fig. 16(a)) are much more intense than in the WN case for $0 < x < 4h$. There is also a plateau for $1h < x < 3h$. This phenomenon was mentioned only in the work of Isomoto and Honami [3] and is not present in the WN simulation. It implies that the plateau is related to the turbulent eddies present in the upstream boundary layer. The plateau could represent the region where the energy of the longitudinal turbulent streaks of the boundary layer is

transferred to spanwise Kelvin-Helmholtz (KH) vortices. Both simulations reach the same maximum of longitudinal turbulent intensity at the same longitudinal position ($x \simeq 4.5h$). Downstream of this maximum, the turbulence intensity becomes larger in the WN case.

The vertical turbulent intensity is also larger in the PS case, but in a much smaller longitudinal region (Fig. 16(b)). The vertical velocity fluctuations becomes larger in the WN case for $x > 2.5h$, and the maximum is also much larger than in the PS case. The maximum of energy is obtained in both cases for $x \simeq 4.5h$. The interesting point is that for both longitudinal and vertical velocity fluctuations, we observe an inversion: the fluctuations becomes larger with the WN case than with the PS case at some point downstream the step. This suggests that the reduction of the recirculation length with the precursor simulation is related to the region just downstream the step edge ($0 < x < 3h$).

VI. INFLUENCE OF UPSTREAM CONDITIONS ON THE FLOW UNSTEADY BEHAVIOR

If the averaged quantities are often discussed in the studies dealing with the backward-facing step, it is more difficult to find references dealing with the unsteady behavior of the flow. In this section we will explore in details how the flow evolves in time and how its spectral signatures are influenced by upstream boundary conditions. We will discuss the fluctuations of global quantities, like the recirculation length, as well as local fluctuations measured on probes located at different positions downstream of the step.

A. Fluctuations of global quantities

1. Skin friction

The time and spatial averaging used to obtain for instance the mean recirculation length X_r can be misleading and give a wrong picture of the flow which is fully 3D and time-dependent. We show on Fig. 17 snapshots of the instantaneous skin friction C_f downstream of the step for the WN case (Fig. 17(a)) and the PS case (Fig. 17(b)). The instantaneous recirculation lengths(averaged in the spanwise directions) are respectively 4.8 h et 5.2 h. When C_f changes of sign it indicates the presence of reverse flow regions. One can see

the main recirculation region and, between the secondary vortex and the step, a small third vortex. The main reverse flow region, and particularly the reattachment line, is very irregular and C_f can reach locally 2 or 3 times its mean value.

2. Recirculation length

To illustrate the oscillations of the mean recirculation length X_r, we show on Fig. 18 a time series of the fluctuations of its spanwise averaged value (as shown on Fig. 17) for both WN (Fig. 18(a)) and PS (Fig. 18(b)) simulations. We add the cumulative average to the time series, to show that the simulations are statistically converged. We can notice the strong fluctuations of X_r, reaching 2.27 h for the WN simulation and 2.61 h for the PS simulation, which is in good agreement with the value (2.5 h) observed by Le et al. [30] in their DNS. They suggest that the sharp drops of X_r are related to the advection of large scale structures in the neighborhood of the reattachment region.

To check this interpretation we recorded pressure fluctuations on a probe located on the wall at the end of the reattachment zone ($x = 7.6h$; $y = 0.2h$). On Fig. 19 we plot together the time series of wall pressure and recirculation length fluctuations. We observe a strong correlation between the sharp drops of the mean recirculation length and the low-pressure events which can be related to the advection of a vortex [31]. This correlation clearly demonstrates that the diminution of the recirculation length is due to the advection of a strong vortical structure.

B. Spectral analysis of local fluctuations

1. Characteristic frequencies

In this section we focus on the modification of the characteristic frequencies of pressure fluctuations recorded in different probes located downstream of the step (Fig. 20), in the shear layer and close to the lower wall downstream of the step. The probes positions are determined as a function of the location of the maximum of longitudinal turbulent intensity [32].

We use a Strouhal number defined as the frequency adimensionalized by the averaged recirculation length, X_r, and the freestream velocity U_0: $St = fX_r/U_0$. Since the flow

is statistically homogenous in the spanwise direction, the spectra are averaged along this direction to ensure statistical convergence. The sampling frequency and the length of the time series give access to Strouhal numbers ranging between 0 and 16, with a 0.020 step. We show on Fig. 21 typical time series of pressure fluctuations recorded on a probe located close to the wall, in the reattachment region (x=5.01 h).

We show on Fig. 22 a typical example of the pressure spectra obtained with different pressure probes in the PS case (figures a, b and c) and the WN case (figures d, e and f). The spectra are adimensionalized by the amplitude of the highest peak obtained for each time series to help the comparison. The first probe is located in the shear layer downstream of the step, the second is further downstream, in the mixing layer, while the third probe is in the reattachment region. The location of the first two probes is slightly different in the PS case than in the WN case to compare the frequencies at the longitudinal location where the amplitude of the peaks is the highest. This is also a first evidence of the effect of the upstream boundary conditions : the longitudinal evolution of the characteristic frequencies is different in the two cases.

The frequencies are rather well defined and the modification of the spectra between the three longitudinal positions is important. If we consider the overall spatial evolution of all the spectra, one can find the main characteristic frequencies of the major phenomena, with dominant high frequencies close to the edge and increasing low frequencies band further downstream. In the following, one should consider a ± 0.05 error bar for all the main frequencies that will be identified in the spectra.

In the shear layer, close to the edge of the step ($x = 1h$), one can see a high frequency around $St = fX_r/U_0 = 1.24$ for the WN case and $St = fX_r/U_0 = 1.63$ for the PS case (Fig. 22(a) and (b)). Considering the probes location, the dominant frequencies can be associated to the Kelvin-Helmholtz (KH) vortices in both cases. This frequency is dominant in the range [0.5h - 1.5h] for the PS case and in the range [2h - 4h] in the WN case. As expected, the incoming boundary layer has a strong influence on the shear-layer instability: if we compare the real frequencies, one find $f_{PS} = 1.7 \times f_{WN}$. The destabilization of the shear layer is clearly triggered by the turbulent boundary layer.

Further downstream in the shear layer, one can see the growth of lower frequencies and especially a peak around $St = 0.94$, for the PS case and the WN case, corresponding to the pairing of the KH vortices (Fig. 22(d) for the PS case and 22(c) for the WN case). This

frequency is dominant in the range [3h - 4h] for the PS case and in the range [4.5h - 5.5h] in the WN case.

Finally, in the reattachment region, two new lower frequencies appear (Fig. 22(e) and 22(f)): one around $St = 0.50 - 0.54$, for both cases, corresponding to the oscillations of the recirculation bubble, and one peak around $St = 0.08$ for the WN case and $St = 0.34$ for the PS case corresponding to the flapping of the shear layer. These results are confirmed by the spectra of wall pressure fluctuations around $X = X_r$ (Fig. 23). The main low frequencies are well measured by the wall probes and the difference between the two simulations is clear. One can see the low frequency peaks around $St = 0.05 - 0.1$ and around $St = 0.5$ for the WN case and the peaks around $St = 0.3$ and $St = 0.5$ for the PS case.

To summarize, the Precursor Simulation leads to higher frequencies than the WN case for the KH vortices and the flapping of the shear layer. On the contrary, the frequencies associated to the pairing of the KH vortices and to the oscillation of the recirculation bubble seem less dependent of the upstream boundary layer. As expected with the modification of the mean flow (smaller recirculation length in the PS case), the spatial evolution of the characteristic frequencies is also different in the two cases.

2. Comparison with previous studies

We report on table II the frequencies for the two simulations together with the frequencies obtained in other experimental or numerical studies of separated flows like the backward-facing step, the separated flow over a Blunt Plate (BP) or a Separated Plate (SP). It seems that the different mechanisms we observed in the backward-facing step are common to all separated flows. For the sake of comparison, the data from the other studies are recalculated using the same definition of the Strouhal number (with X_r as a characteristic length).

Our results compare reasonably well with the one observed in the previous studies, even if no one ever characterized the four frequencies. In fact, the oscillation of the recirculation bubble is the only phenomenon that has been observed in all the studies (BFS, BP and SP), with a mean Strouhal number $< St_{exp} >= 0.67$ for the experiments and $< St >_{num}= 0.543$ for the numerical simulation. Our results correspond to the average of the other numerical studies which tend to underestimate this frequency compared to the experimental results. The dispersion observed for the frequency associated with the KH vortices can be explained

by the high sensitivity to upstream perturbations: it can be triggered if the shear layer is excited by a perturbation with the proper frequency [33]. The large difference between the PS and WN case is a clear proof of this mechanism which can be explained by the relatively broad frequency spectrum of the incoming upstream turbulent boundary layer in the PS case. The same kind of explanation can be applied to the frequency associated to the flapping of the shear layer. A more physical description of the destabilization of the shear layer will be detailed in the following section. The pairing of the KH vortices seems to have a typical Strouhal number around $[0.9 - 1.1]$.

3. Influence of the upstream flow condition

To conclude the study, we wish to emphasize the role of the coherent structures contained in the incoming boundary layer on the shear layer. We show on Fig. 24 an instantaneous visualization of the flow structure just upstream and downstream the step edge for both WN (a) and PS (b) case. The flow comes from bottom to top and the horizontal arrow on the left of the pictures shows the step edge.

On Fig. 24(a), we see no trace of coherent structures upstream of the step edge while we can see a large quasi-2D KH vortex at $X = 2h$ downstream of the step edge. On the opposite, Fig. 24(b) exhibits clear signatures of longitudinal vortices upstream of the step edge. The spanwise modulation of the isocontours of longitudinal velocity fluctuations u'/U_o is typical of turbulent streaks with alternatively high (black) and low (grey) longitudinal velocities. Just downstream of the step edge we notice a strong correlation between the accelerated / decelerated regions and the modulation of the KH vortices. It seems that the natural spanwise modulation of the longitudinal velocity is responsible for the rapid destabilization of the shear layer. This has to be compared to the control experiments of Sung et al. [34] who performed blowing and suction on the step edge. Depending on the parameters, they observed a strong modification of the recirculation length. Our result is also interesting in the perspective of flow control as it confirms the potentiality of spanwise longitudinal velocity modulation to reduce the recirculation length.

We want to emphasize also the persistence of the longitudinal vortices. The visualization of Fig. 25 is an extension of Fig. 24(b), without the Q-criterion isosurfaces so that we can see the high and low longitudinal velocity streaks before and after the step edge. Despite

the disorder observed in the visualization, we can follow the spanwise modulation up to 3 to 4 h after the step. It confirms the strength of the incoming upstream longitudinal vortices and their role in the destabilization of the shear layer.

VII. CONCLUSION

In this study , LES of the flow over a backward-facing step have been used to to investigate the influence of upstream boundary conditions on the development of turbulent structures. The first inlet condition consists of a mean turbulent profile perturbed by a white noise (WN). This is compared to a second more realistic conditions, in which fully turbulent inflow data are derived from an auxiliary simulation of a quasi-temporal boundary layer (precursor simulation, PS).

We have carried out an analysis of the unsteady behavior of the separated flow downstream the step. Thanks to the pressure fluctuation time series we could identify the characteristic frequencies associated to the main instability mechanisms occurring in the shear layer and the recirculation bubble. Pressure statistics, supplemented by visualizations of structures, demonstrate how the flow in the separated layer is strongly influenced by the upstream conditions. In the case where the inlet stemmed from a precursor simulation, we have shown that the incoming turbulent structures significantly influence the flow development downstream of the step. We have observed in particular how the streaks and the quasi-longitudinal vortices trigger a rapid destabilization of the mixing layer resulting in a shortening of the recirculation length. We have shown in the PS case that the incoming boundary layer is modulated in the spanwise direction with alternate high (inflow) and low (outflow) longitudinal velocity regions. The modulation can be compared to a randomized blowing and suction experiments. It results in a destabilization of the Kelvin-Helmholtz (KH) vortices shed behind the step inducing a shortening of the recirculation length.

The time-frequency spectra of pressure fluctuations in different positions downstream of the step edge are also strongly modified. They are much richer in the PS case and one can also observe an ultraviolet shift of some of the characteristic peaks, like the one associated to KH vortices. The spatial distribution of the frequencies is also significantly modified. It illustrates the essential role of proper upstream conditions to correctly simulate the structure and dynamics of spatially-developing separated flows. This will be even more critical if the

objective is the simulation of a flow controlled by steady or time-dependent perturbations.

Acknowledgments

We wish to acknowledge Y. Dubief, F. Delcayre and P. Begou for their help.

[1] L. Davidson S. Krajnovic. Large eddy simulation of the flow around an Ahmed body. In *Proceedings of the 2004 ASME Heat Transfer/Fluids Engineering Summer Conference*, number HT-FED2004-56325.

[2] E. Sergent. Specification of les inlet boundary conditions using vortex method, 2002. Thèse de Doctorat de l'Ecole Centrale de Lyon.

[3] K. Isomoto and S. Honami. The effect of inlet turbulence intensity on the reattachment process over a backward-facing step. *J. Fluids Engng.*, **111**:87–92, 1989.

[4] E. Balaras H.-J. Kaltenbach A. Keating, U. Piomelli. A priori and a posteriori tests of inflow conditions for large-eddy simulation. *Phys. Fluids*, **16**:4696–4712, 2004.

[5] A. Silveira Neto, D. Grand, O. Métais, and M. Lesieur. A numerical investigation of the coherent vortices in turbulence behind a backward-facing step. *J. Fluid Mech.*, **256**:1–25, 1993.

[6] F. Ducros, P. Comte, and M. Lesieur. Large-eddy simulation of transition to turbulence in a boundary layer developing spatialy over a flat plate. *J. Fluid Mech.*, **326**:1–36, 1996.

[7] P. Comte, J. H. Silvestrini, and P. Bégou. Streamwise vortices in large-eddy simulations of mixing layers. *Eur. J. Mech., B/Fluids*, **17**(4):615–639, 1998.

[8] S. Lee, S. K. Lele, and P. Moin. Simulation of spatially evolving turbulence and the applicability of Taylor's hypothesis in compressible flow. *Phys. Fluids A*, **4**(7):1521–1530, 1992.

[9] H. Le, P. Moin, and J. Kim. Direct numerical simulation of turbulent flow over a backward-facing step. *J. Fluid Mech.*, **330**:349–374, 1997.

[10] Ph. Druault, E. Lamballais, J. Delville, and J. P. Bonnet. Development of experiment/simulation interfaces for hybrid turbulents results analysis via the use of DNS. *Turbulence and Shear Flows*, **1**:779–784, 1999.

[11] U. Piomelli, J.-L. Balint, and J. M. Wallace. On the validity of Taylor's hypothesis for wall-bounded flows. *Phys. Fluids A*, **1**(3):609–611, 1988.

[12] Y. Na and P. Moin. The structure of wall-pressure fluctuations in turbulent boundary layers with adverse pressure gradient and separation. *J. Fluid Mech.*, **337** :347–373, 1998.

[13] Y. M. Chung and H. J. Sung. Comparative study of inflow conditions for spatially evolving simulation. *AIAA Journal*, **35**(2):269–274, 1997.

[14] P. R. Spalart. Direct numerical simulation of a turbulent boundary layer up to $Re_\theta = 1410$. *J. Fluid Mech.*, **187**:61–98, 1988.

[15] P. R. Spalart and J. H. Watmuff. Experimental and numerical study of a turbulent boundary layer with pressure gradient. *J. Fluid Mech.*, **249**:337–371, 1992.

[16] R. Friedrich and M. Arnal. Analysing turbulent backward-facing step flow with the lowpass-filtered Navier-Stokes equations. *J. Wind Engng and Ind. Aerodyn.*, **35**:101–128, 1990.

[17] N. Li, E. Balaras, and U. Piomelli. Inflow conditions for large eddy-simulation of mixing layers. *Phys. Fluids A*, **12**(4):535–538, 2000.

[18] T. Lund, X. Wu, and K. D. Squires. Generation of turbulent inflow data for spatially-developping boundary layer simulations. *J. Comp. Phys.*, **140**:233–258, 1998.

[19] O. Métais and M. Lesieur. Spectral large eddy simulation of isotropic and stably stratified turbulence. *J. Fluid Mech.*, **239**:157–194, 1992.

[20] P. Comte M. Lesieur, O. Métais. *Large-eddy simulations of turbulence*. Cambridge University Press, 2005.

[21] S. Jovic and M. Driver. Backward-facing step measurements at low Reynolds number, Re_h=5000. *Rep.* TM-108807, NASA, 1994.

[22] D. Gottlieb and E. Turkel. Dissipative two-four methods for time dependant problems. *Math. Comp.*, **30**(136):703–723, 1976.

[23] Y. Dubief. Simulation des grandes échelles de la turbulence de la région de proche paroi et des écoulements décollés, 2000. Thèse de Doctorat de l'Institut National Polythechnique de Grenoble.

[24] K. W.Thompson. Time dependent boundary conditions for hyperbolic systems. *J. Comp. Phys.*, 68:506–517, 1987.

[25] K. W. Thompson. Time dependent boundary conditions for hyperbolic systems, II. *J. Comp. Phys.*, 89:439–461, 1990.

[26] C. Fureby. Large eddy simulation of rearward-facing step flow. *AIAA Journal*, **37**(11):1401–1410, 1999.

[27] D. M. Kuehn. Effects of adverse pressure gradient on the incompressible reattaching flow over a rearward-facing step. *AIAA Journal*, **18**(3):343–344, 1980.

[28] D. M. Driver, H. L. Seegmiller, and J. G. Marvin. Time-dependant behavior in a reattaching shear layer. *AIAA Journal*, **25**(7):914–919, 1987.

[29] C. Chandrsuda and P. Bradshaw. Turbulence structure of reattaching mixing layer. *J. Fluid Mech.*, **110**:171–194, 1981.

[30] H. Le and P. Moin. Direct simulation of turbulent flow over a backward-facing step. *Rep.* TF-58, Thermosciences Division, Dept. of Mech. Engng, Stanford University, 1994.

[31] Y. Couder, O. Cadot and S. Douady. Characterization of the low-pressure filaments in a three-dimensional turbulent shear flow. *Phys. Fluids*, **7**:4696–4712, 1995.

[32] M. Kiya and K. Sasaki. Structure of a turbulent separation bubble. *J. Fluid Mech.*, **137**:83–114, 1983.

[33] J. Silvestrini. Simulations des grandes échelles des zones de mélanges; application à la propulsion solide des lanceurs spatiaux, 1996. Thèse de Doctorat de l'Institut National Polytechnique de Grenoble.

[34] K. B. Chun and H. J. Sung. Effect of spanwise-varying local forcing on turbulent separated flow over a backward-facing step. *Exp. Fluids*, **26**:437–440, 1999.

[35] J. K. Eaton and J. P. Johnston. Low frequency unsteadyness of a reattaching turbulent shear layer. *Turbulent Shear Flows*, **3**:162–170, 1982.

[36] N.J. Cherry, R. Hillier, and M. E. M. P. Latour. Unsteady measurements in a separated and reattaching flow. *J. Fluid Mech.*, **144**:13–46, 1984.

[37] F. W. Roos and J. K. Kegelman. Control of coherent structures in reattaching laminar and turbulent shear layer. *AIAA Journal*, **24**(12):1956–1963, 1986.

[38] I. P. Castro and A. Haque. The structure of a turbulent shear layer bounding a separated region. *J. Fluid Mech.*, **179**:439–468, 1987.

[39] M. Kiya. Separation bubbles. In P. Germain, M. Piau, and D. Caillerie, editors, *Theoretical and Applied Mechanics*, pages 173–191. Elsevier Science publishers B. V., North-Holland, 1989.

[40] W. J. Devenport and E. P. Sutton. Near-wall behavior of separated and reattaching flows. *AIAA Journal*, **29**(1):25–31, 1991.

[41] D. K. Tafti and S. P. Vanka. A three dimentional numerical study of flow separatiom and reattachment on a blunt plate. *Phys. Fluids A*, **3**:12, 1991.

[42] A. Suksangpanomrung, N. Djilali, and P. Moinat. Large-eddy simulation of separated flow over a bluff-body rectangualr plate. *Int. J. Heat and Fluid Flow*, **21**:655–663, 2000.

[43] M. Arnal and R. Friedrich. Large Eddy Simulation of a turbulent flow with separation.

Turbulent Shear Flows, 8:169, 1993.

[44] F. Delcayre. Etude par la Simulation des Grandes Echelles d'un écoulement décollé : la marche descendante, 1999. Thèse de Doctorat de l'Institut National Polythechnique de Grenoble.

List of Tables

Data/Run	WN	PS
$(N_i)_{inlet}$	(21, 57, 61)	id
$(N_i)_{step}$	(125,72,61)	id
$(\Delta_i)^+$	(4-66,1.3-50,17)	id
$(L_x)_{step}$	18h	18h
Inflow data	White Noise	Precursor Simulation
Upper condition	Outflow	Outflow
X_r/h	5.8	5.29

TABLE I: Characteristic parameters in the two simulations

Reference	Geometry	Flapping	X_r oscillation	Pairing KH	KH
Eeaton & Johnston (1982)[35]	BFS	0.152	0.52	-	-
Cherry et al. (1984) [36]	BP	0.1	0.6	-	-
Roos & Kegelman (1986) [37]	BFS	-	≤ 0.68	1.1	2.2
Castro & Haque (1987) [38]	SP	0.12	0.6	-	-
Driver et al. (1987) [28]	BFS	0.12	0.7	-	-
Kiya (1989) [39]	BP	$\leq$0.2 (0.12)	0.6-0.7	-	-
Devenport & Sutton (1991)[40]	BFS	0.18	0.74	-	-
Tafti & Vanka (1991) [41]	BP	0.1-0.35 (0.15)	0.5-0.7 (0.6)	1.13-1.42 (1.2)	1.9-2.33 (2.1)
Suksangpanorung et al. (2000) [42]	BFS	0.086-0.215	0.284- 0.86	-	-
Arnal & Friedrich (1991) [43]	BFS	0.07-0.3	0.5- 0.7	-	2
Silveira et al. (1993) [5]	BFS	-	0.65	-	-
Le & Moin (1994) [30]	BFS	-	0.38	-	-
Delcayre (1999) [44]	BFS	-	0.5	0.93	1.63
White Noise	BFS	0.08	0.50	0.94	1.24
Precursor simulation	BFS	0.34	0.54	0.94	1.63

TABLE II: Typical frequencies observed in separated-reattached flows : $St = fX_r/U_0$. Data unknown : - . BFS : Backward-Facing Step; BP : Blunt Plate; SP : Separated Plate. The upper part of the table corresponds to experimental results and the lower part correspond to numerical simulations.

List of Figures

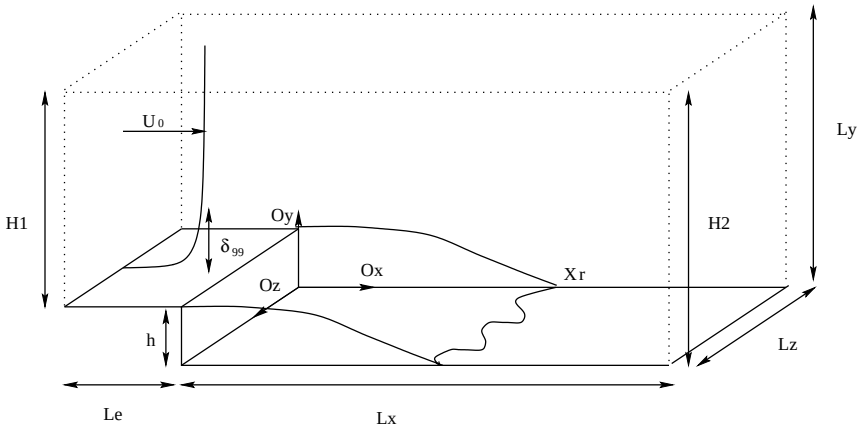

FIG. 1: Description of the computational domain.

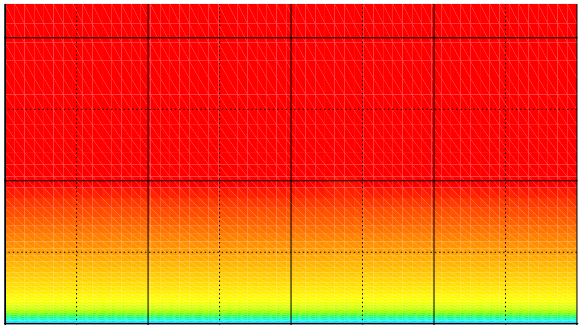

(a)

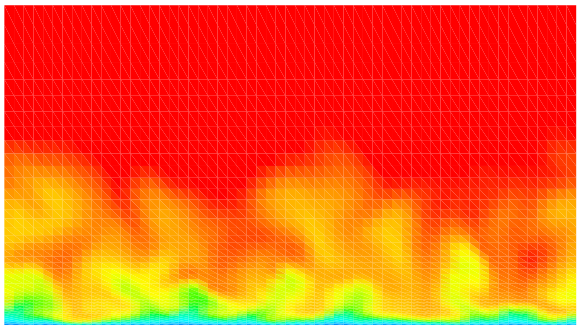

(b)

FIG. 2: (Color online) Visualization of the instantaneous longitudinal adimensionalized velocity field in the cross-section just upstream of step edge. (a) : WN, (b) : PS.

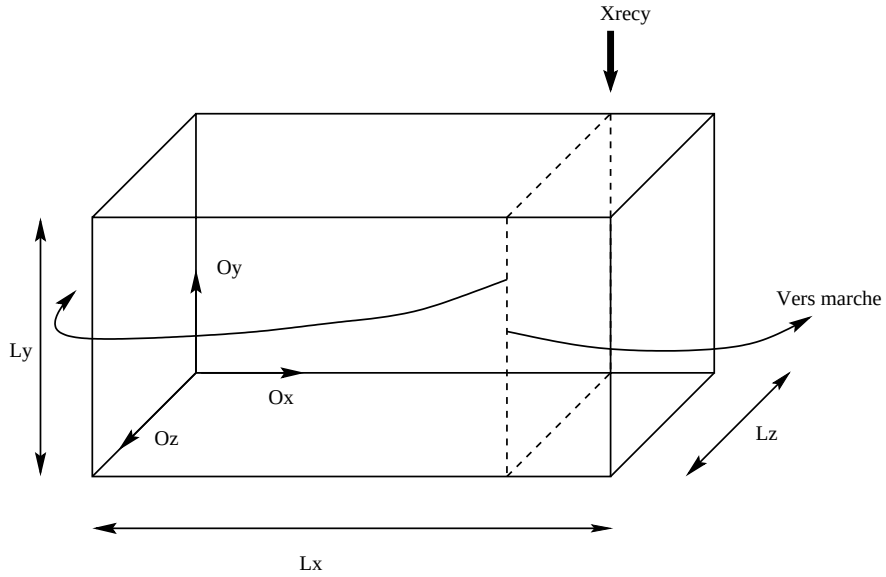

FIG. 3: Description of the precursor domain. The data are taken in the plane $X_{recy} = 8h$ ($L_x = 10h$) to be used as inlet boundary for the main domain computation and for the precursor domain.

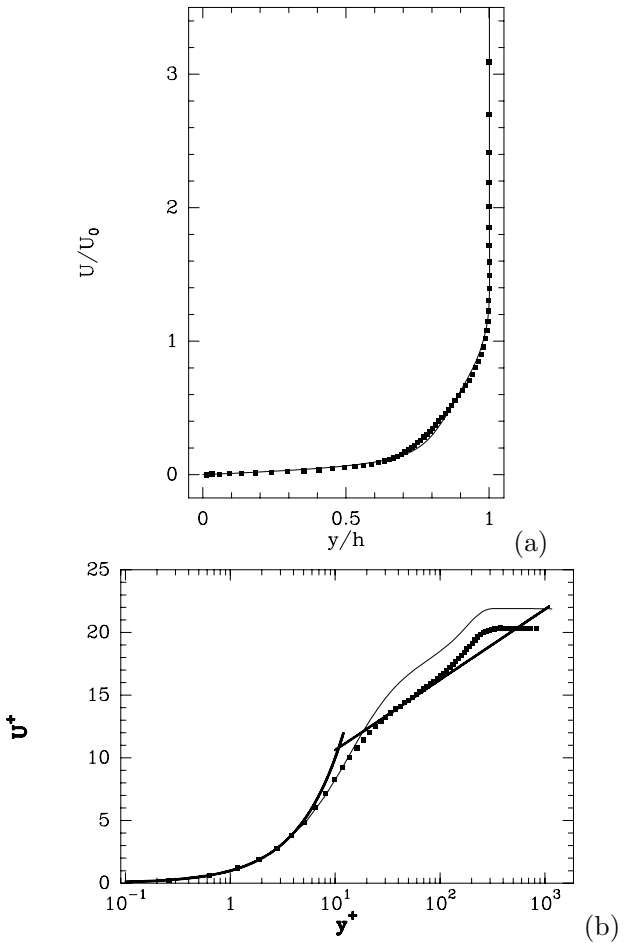

FIG. 4: Mean longitudinal velocity at recycling position: ——: present results, ■: [14], ——: $(u^+ = y^+, u^+ = \frac{1}{0.41} log y^+ + 5.0)$. (a): in step unit; (b): in wall unit.

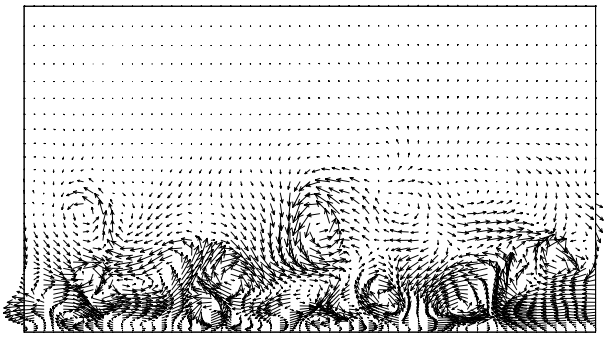

FIG. 5: Projection of velocity vectors in the cross-section of the outlet of the precursor domain. One can clearly see the longitudinal vortices strongly interacting in the turbulent boundary layer.

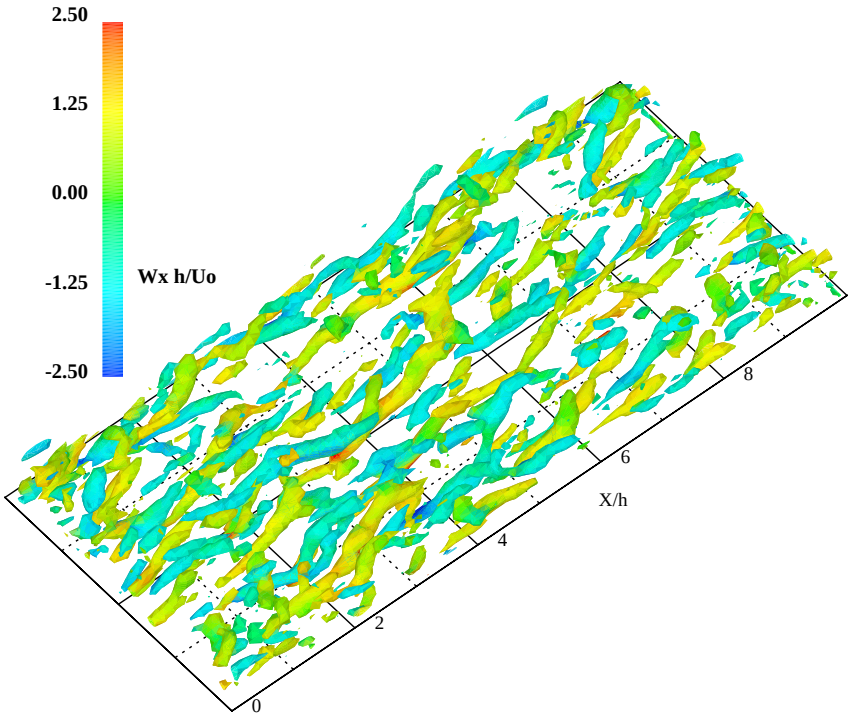

FIG. 6: (Color online) Isosurface of the second invariant of the velocity gradient($Q = 0.5{U_o}^2/h^2$) colored by longitudinal vorticity in the precursor domain

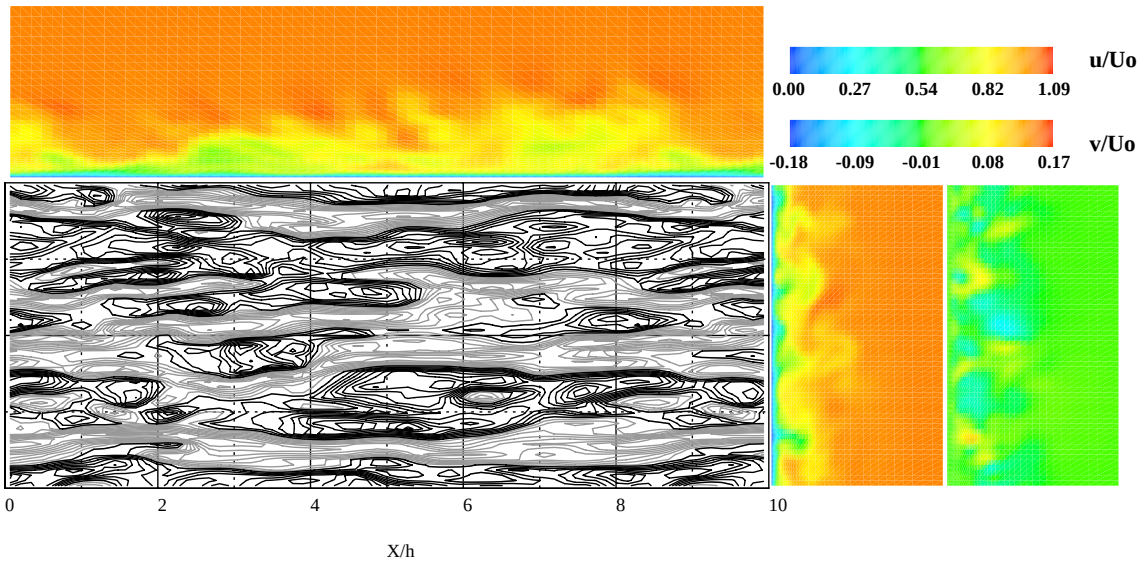

FIG. 7: (Color online) Contours of the instantaneous longitudinal velocity fluctuations in an horizontal plane close to the wall ($y = 0.054h$) in the precursor domain. In black: $0 \leq \frac{u'}{U_o} \leq 0.3$; in grey: $-0.3 \leq \frac{u'}{U_o} \leq 0$. The upper view is a longitudinal cross-section. The figures on the right side are cross-sections of longitudinal and vertical velocity at the outlet of the Precursor Domain.

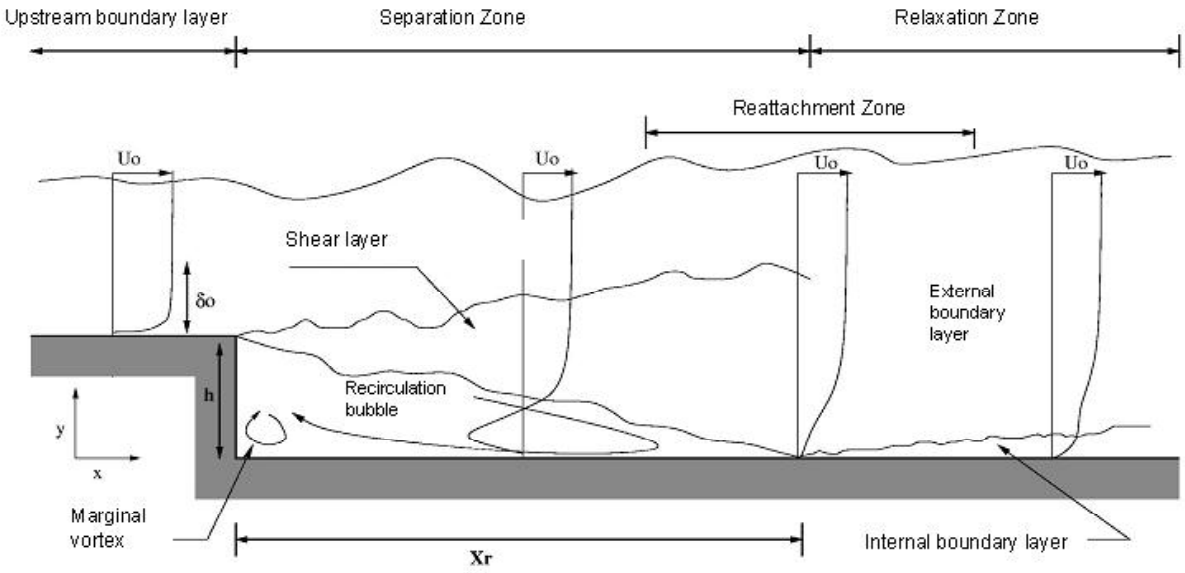

FIG. 8: Simplified representation of the main physical phenomena downstream of the BFS.

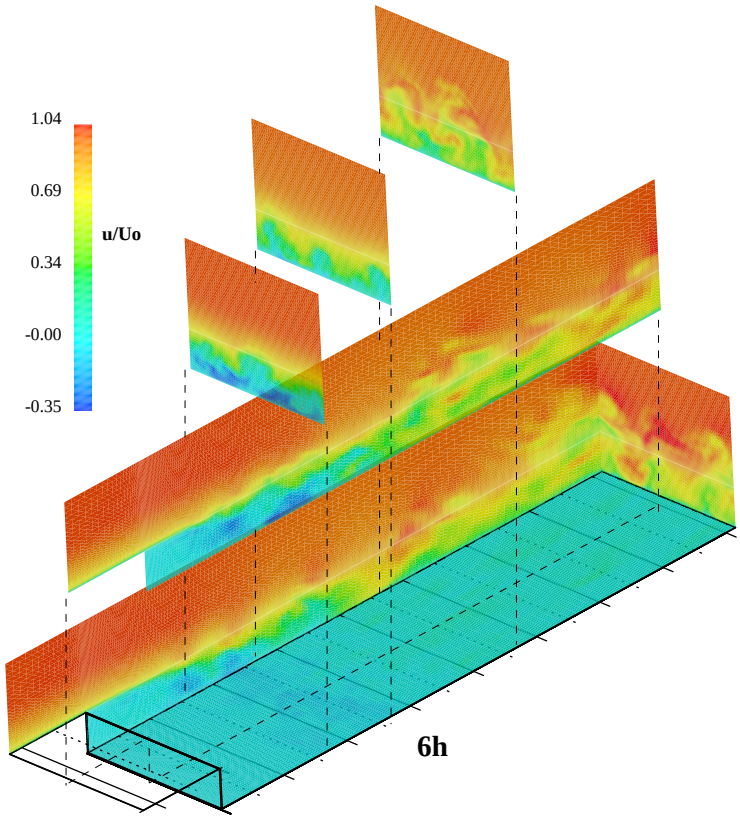

(a)

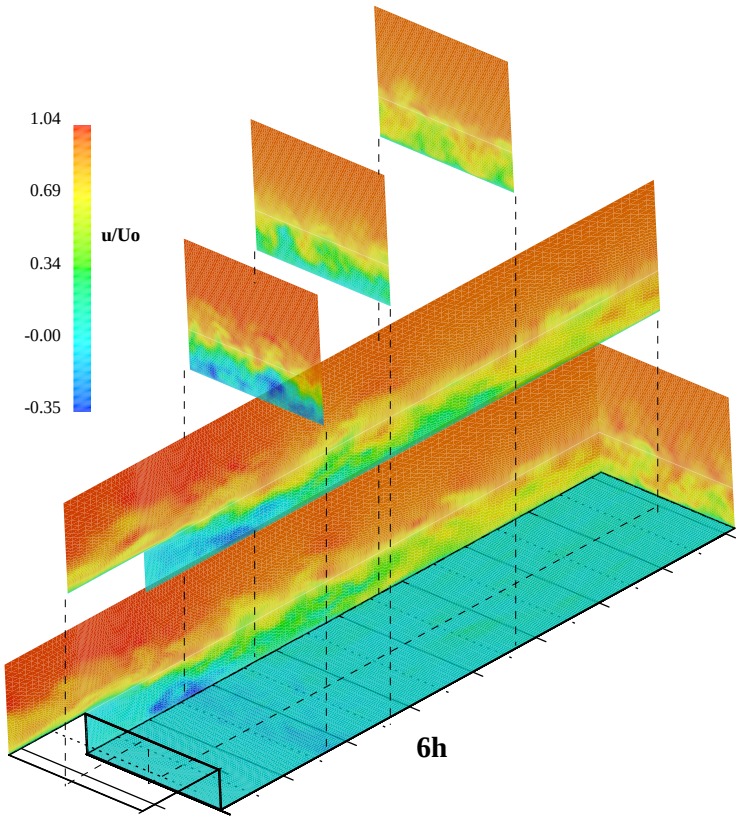

(b)

FIG. 9: (Color online) Visualization of the instantaneous longitudinal velocity field in different cross-sections of the domain. (a) : WN, (b) : PS.

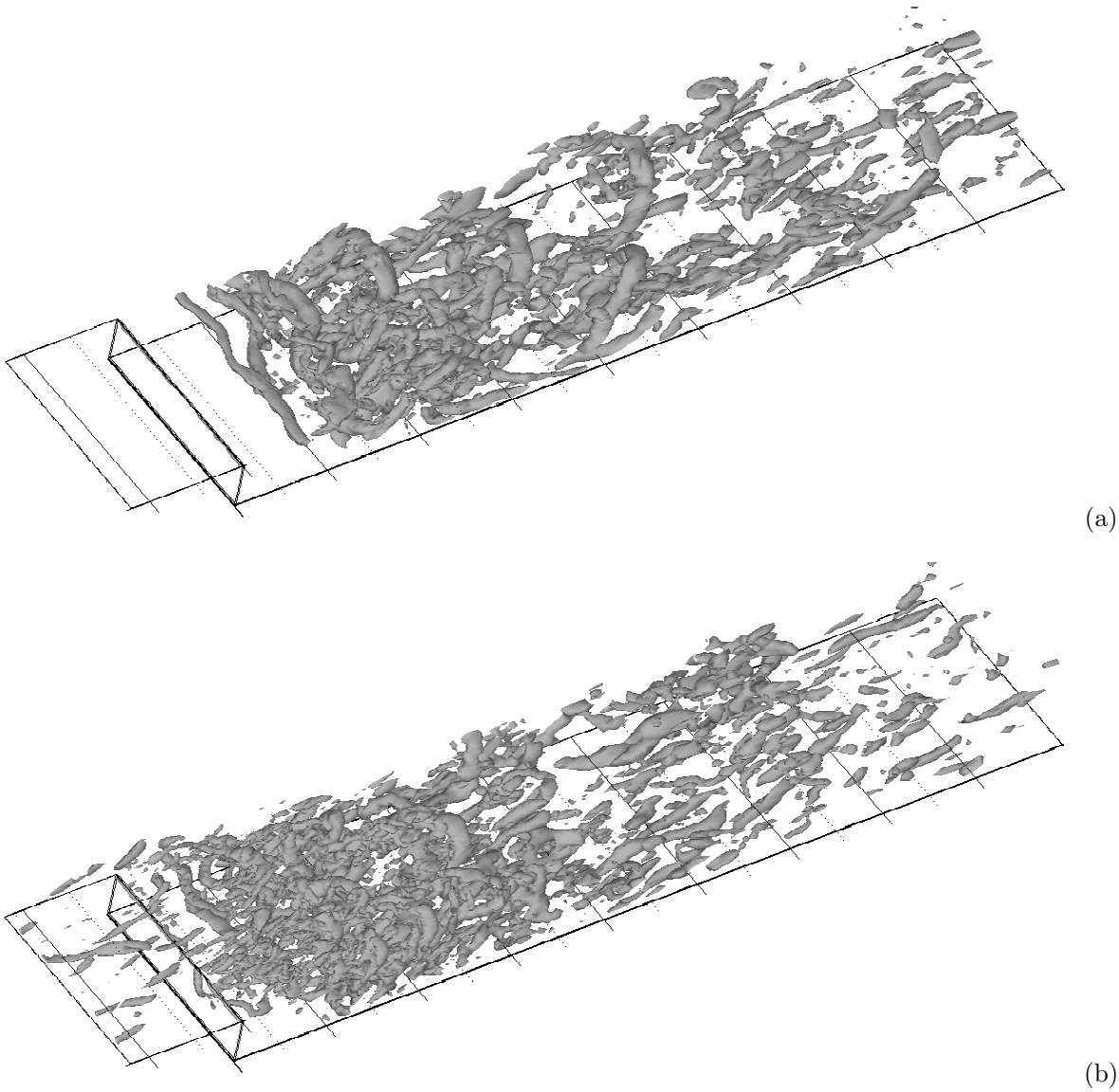

(a)

(b)

FIG. 10: Visualization of the vortices through isosurfaces of Q-criterion. (a) : WN, (b) : PS.

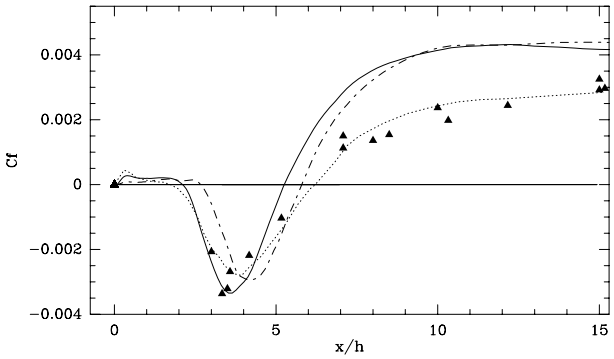

FIG. 11: Friction coefficient : ▲ : Jovic and Driver (1994) [21]; ··· : Le et al (1997) [9], -·- : White Noise; — : Precursor Simulation

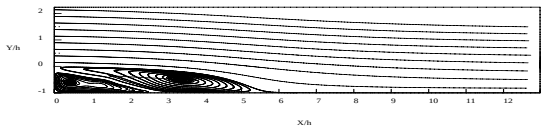

(a)

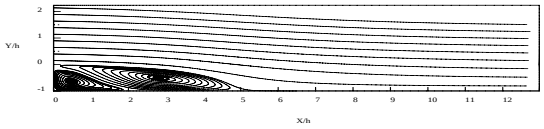

(b)

FIG. 12: Stream-function contours of the mean flow (averaged in time and space) for the two simulations. (a) : WN, (b) : PS. We can see the shortening of the recirculation bubble with a more realistic boundary layer.

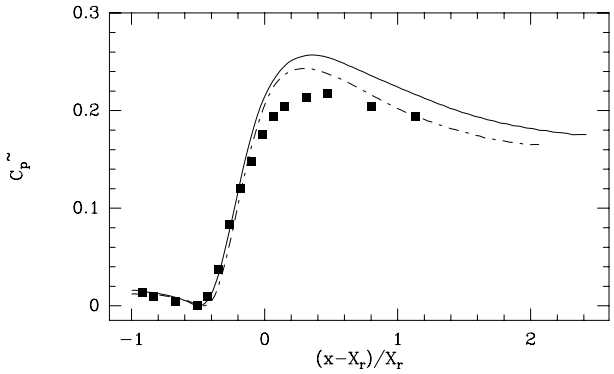

FIG. 13: Longitudinal profile of the mean pressure coefficient $\widetilde{C_p} = \frac{C_p - C_{p,min}}{1 - C_{p,min}}$. ■: Driver et al. [28]; -·- : WN; — : PS.

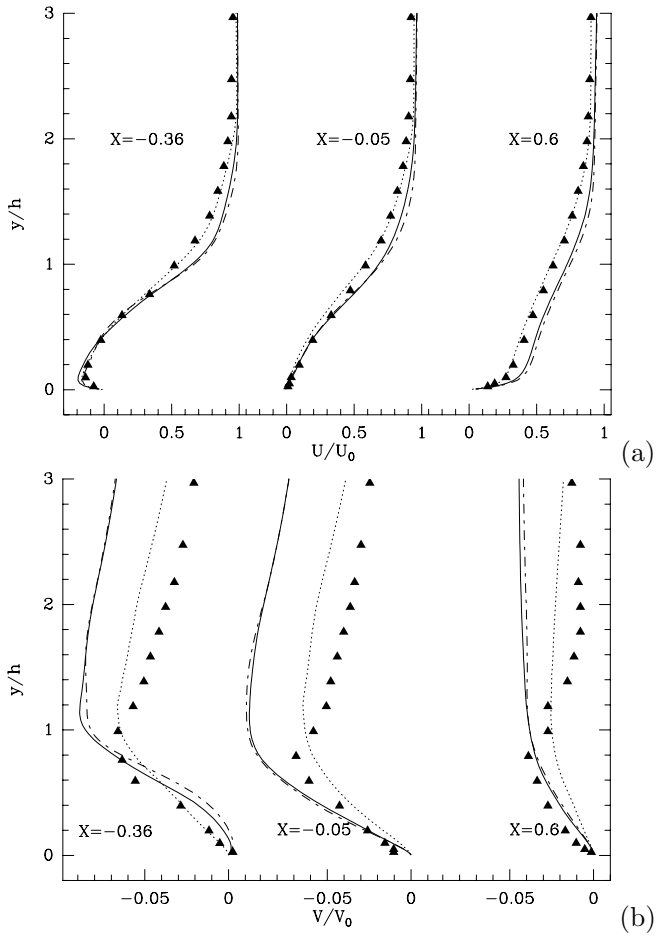

FIG. 14: Mean longitudinal (a) and vertical (b) velocity profiles at three different streamwise positions downstream of the step. ▲ : Jovic and Driver [21]; ··· : Le et al. [9]; -·- : WN; — : PS.

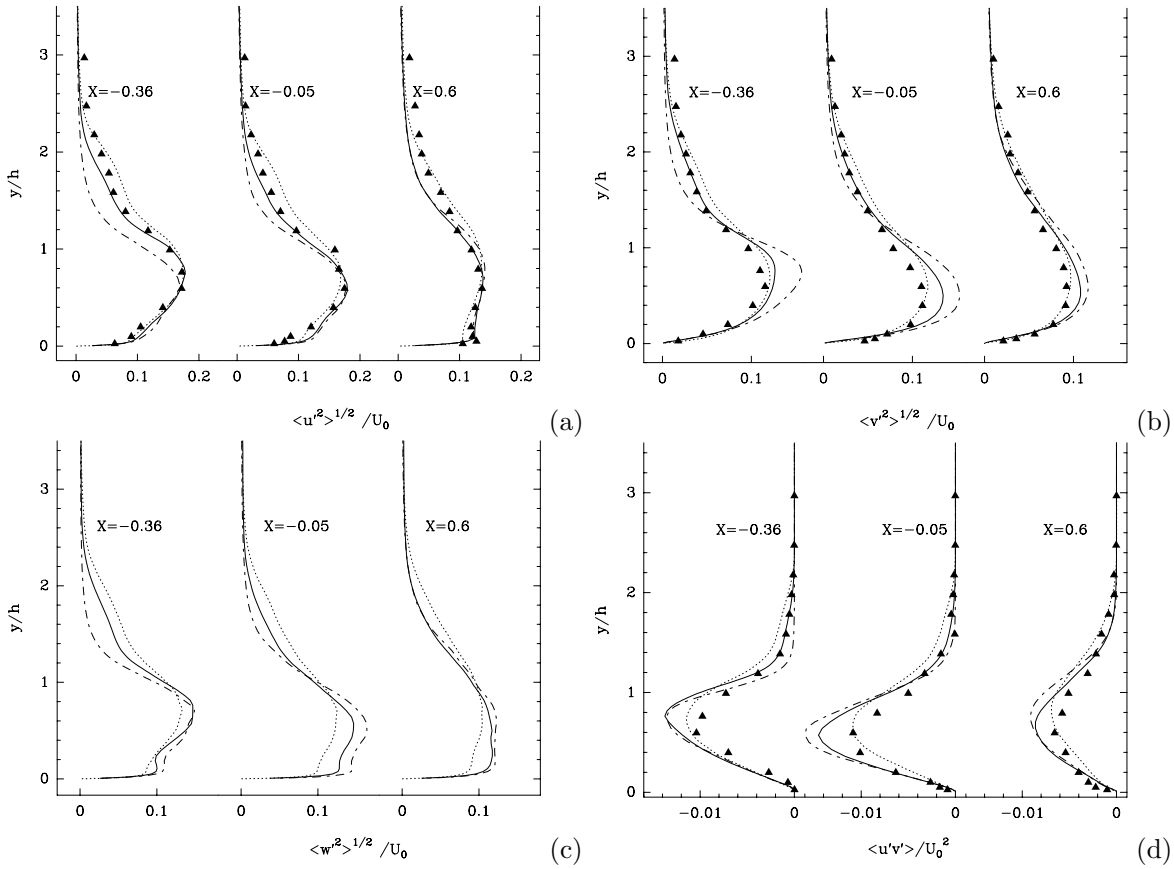

FIG. 15: Comparison of Reynolds stress verticale profiles for three different streamwise positions. (a) $< u'^2 >^{1/2} /U_o$, (b) $< v'^2 >^{1/2} /U_o$, (c) $< w'^2 >^{1/2} /U_o$, (d) $< u'v'^2 >^{1/2} /U_o^2$. ▲ : Jovic and Driver [21]; $\cdots$: Le et al. [9]; -·- : WN; — : PS.

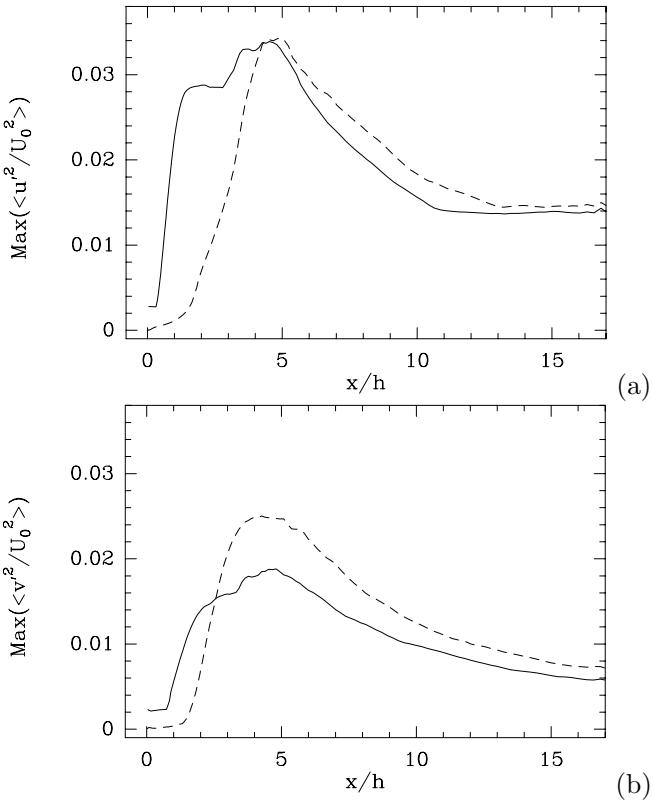

FIG. 16: Longitudinal evolution of the maxima of longitudinal (a) and vertical (b) turbulent intensities. $\cdots$: WN; — : PS.

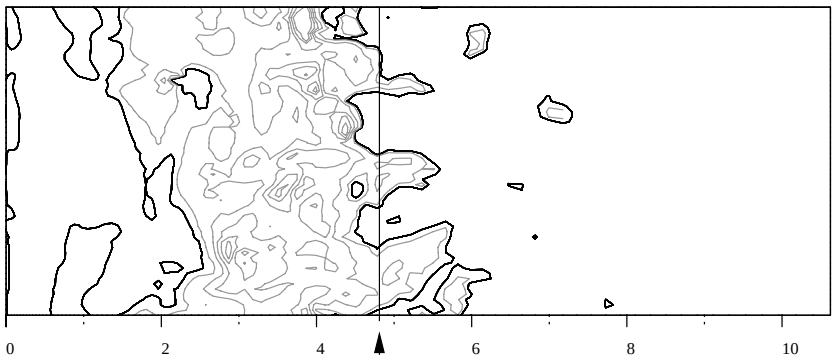

(a)

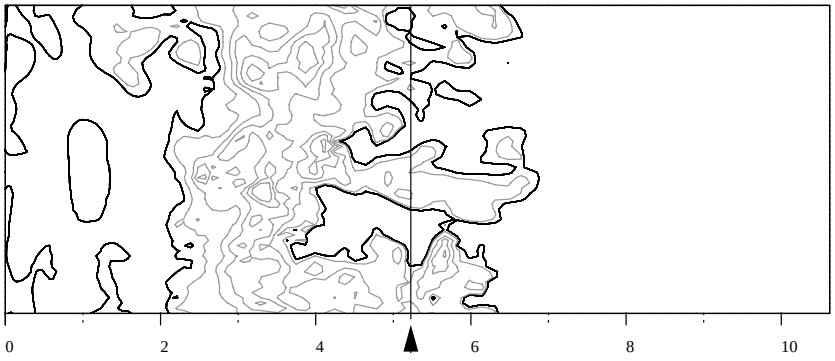

(b)

FIG. 17: Contours of instantaneous skin friction coefficient downstream of the step at time $t = 186\,U_0/h$, for the WN case (a) and at time $t = 199\,U_0/h$, for the PS case (b). Black line : $C_f = 0$, gray line : $-7.5\,10^{-3} \leq C_f < 0$, $|\Delta C_f| = 1.5\,10^{-3}$. The arrow indicates X_r.

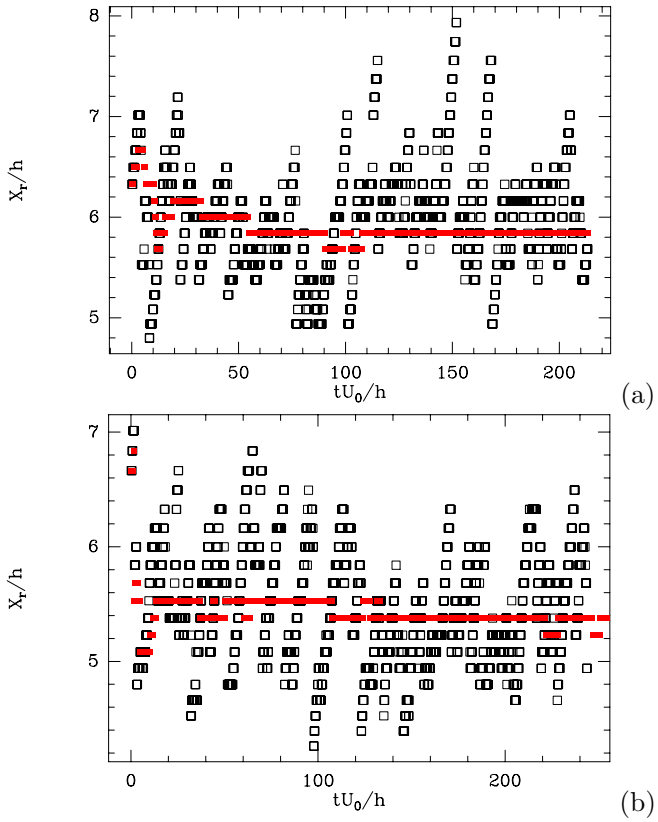

FIG. 18: (Color online) □ : Time series of instantaneous recirculation length (spanwise averaged). ■ : Evolution of the cumulative average. (a): WN, (b): PS.

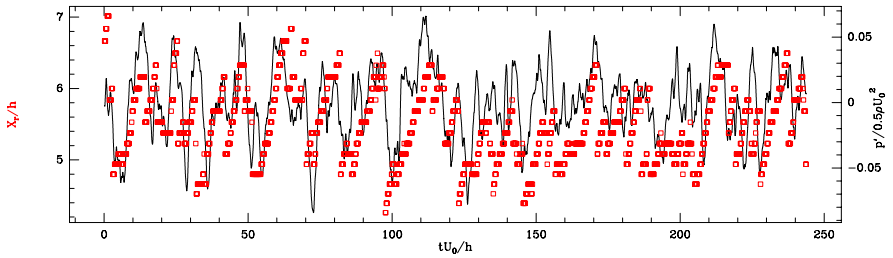

FIG. 19: (Color online) Time series of the recirculation length X_r (□) and of the fluctuation of wall pressure (—) at the end of the mean reattachment zone ($x = 7.6h; y = 0.2h$), Precursor Simulation.

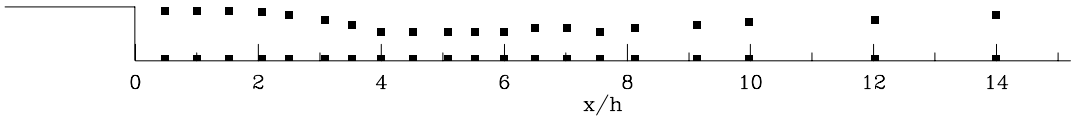

FIG. 20: Localization of the pressure probes downstream of the step (WN and PS) along the shear layer, at the vertical position where the longitudinal turbulence intensity is maximum, and close to the wall.

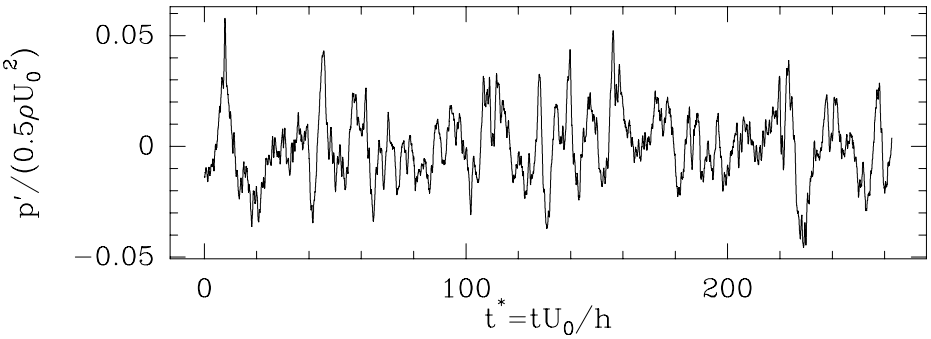

FIG. 21: Time series of pressure close to the wall in the reattachment region ($x = 5.01h$, $y = 0.0052h$).

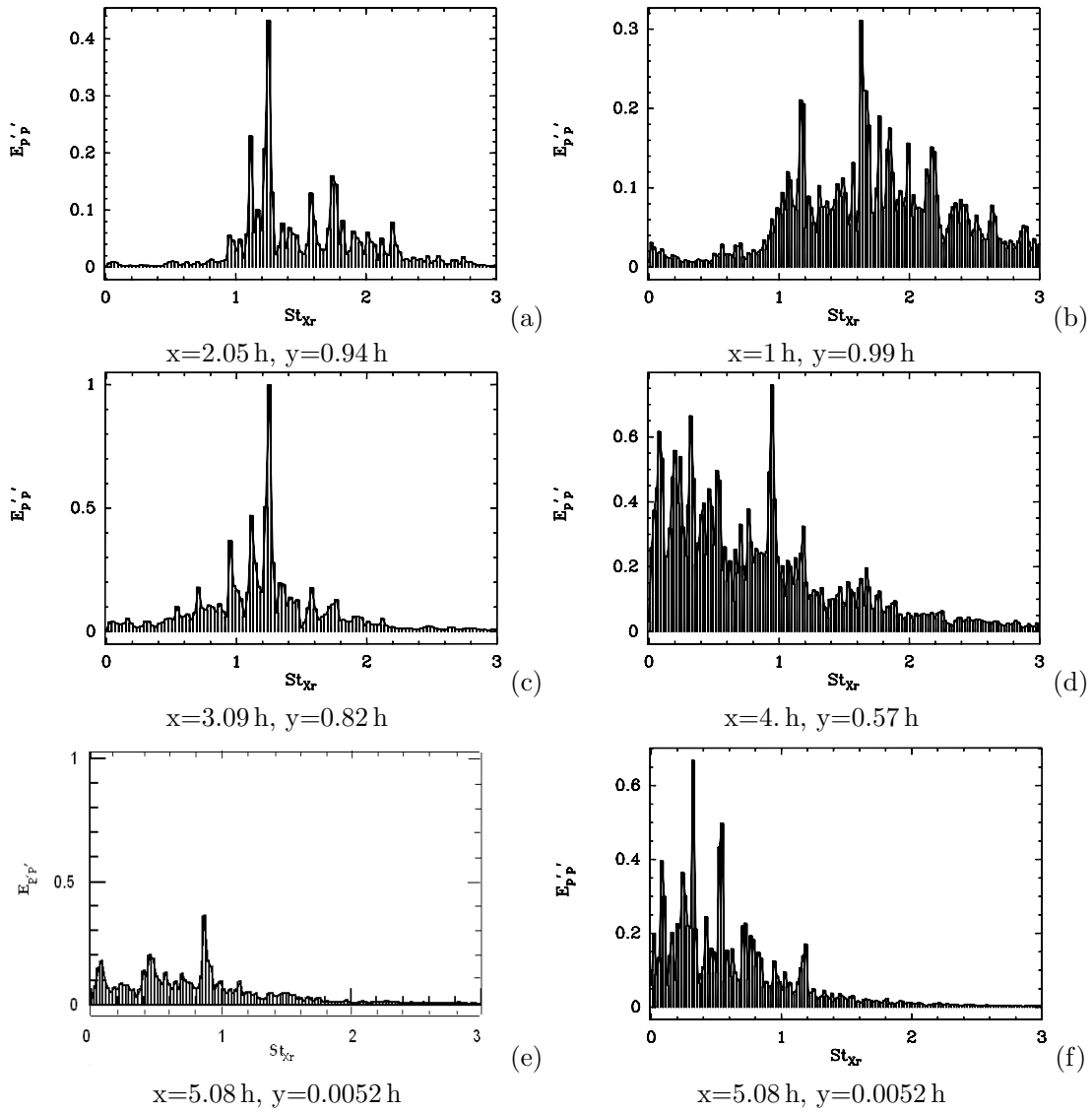

FIG. 22: Examples of spectra of local pressure fluctuations in three positions in the domain downstream of the step in the WN (a, c, e) and PS cases (b, d, f) : (a, b) in the shear layer downstream of the step, (c, d) further downstream in the shear layer, (e, f) in the reattachment region. To make the comparison easier, we do not use the same probes in the figures a) and b) as well as in the figures c) and d).

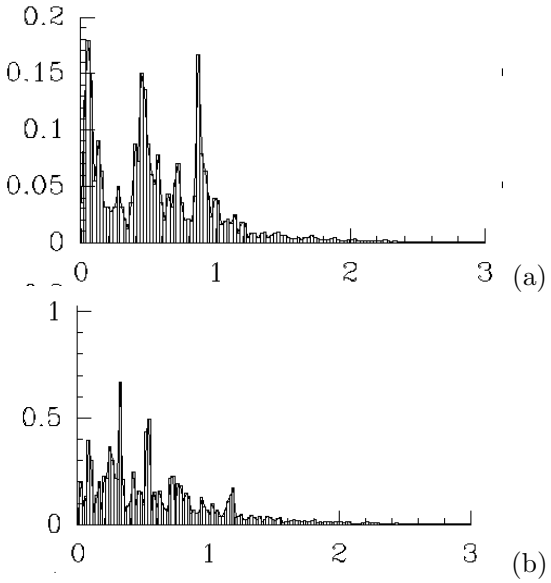

FIG. 23: Comparison of the spectra of wall pressure fluctuations for the WN case (a) and the PS case (b).

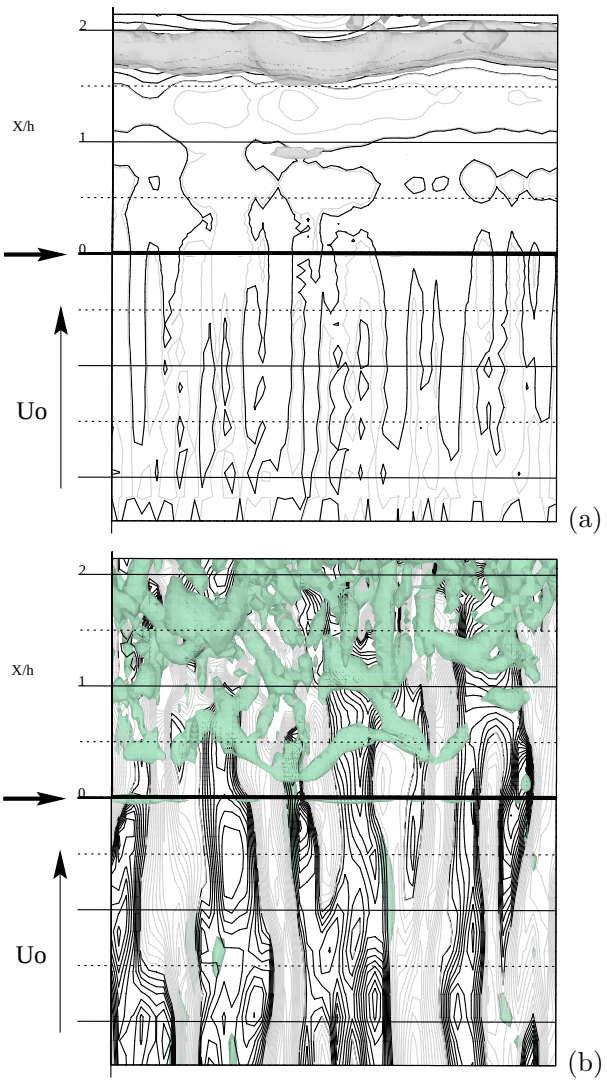

FIG. 24: (Color Online) Upper view of the instantaneous contours of longitudinal velocity fluctuations close to the wall ($y^+ \sim 12$) together with isosurface of Q criterion $Q = 0.8U_0^2/h^2$. Black : $0 \leq u'/U_0 \leq 0.3$, grey : $-0.3 \leq u'/U_0 \leq 0$, $|\Delta u'/U_0| = 0.021$. (a) : WN, (b) : PS. The horizontal arrow on the left of the pictures indicates the step edge.

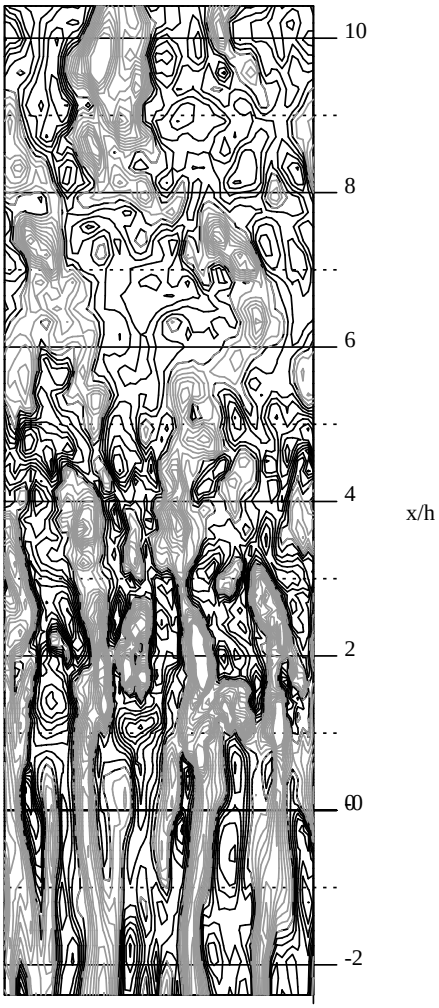

FIG. 25: Isocontours of instantaneous longitudinal velocity fluctuations in the plane $y^+ \sim 12$ above the wall, upstream and downstream of the step edge in the PS case. The flow goes from bottom to top. Black : $0 \leq u'/U_0 \leq 0.35$, Grey : $-0.35 \leq u'/U_0 \leq 0$, $|\Delta u'/U_0| = 0.031$.